

Automatic detection of A-line in lung ultrasound images using deep learning and image processing

Wenyu Xing^{1,2} | Guannan Li³ | Chao He⁴ | Qiming Huang⁵ | Xulei Cui⁶ |
Qingli Li³ | Wenfang Li⁴ | Jiangang Chen^{3,7} | Dean Ta^{1,8}

¹Center for Biomedical Engineering, School of Information Science and Technology, Fudan University, Shanghai, China

²Human Phenome Institute, Fudan University, Shanghai, China

³Shanghai Key Laboratory of Multidimensional Information Processing, East China Normal University, Shanghai, China

⁴Department of Emergency and Critical Care, Changzheng Hospital, Naval Medical University, Shanghai, China

⁵School of Advanced Computing and Artificial Intelligence, Xi'an Jiaotong-liverpool University, Suzhou, China

⁶Department of Anesthesiology, Peking Union Medical College Hospital, Chinese Academy of Medical Sciences, Beijing, China

⁷Engineering Research Center of Traditional Chinese Medicine Intelligent Rehabilitation, Ministry of Education, Shanghai, China

⁸Department of Rehabilitation Medicine, Huashan Hospital, Fudan University, Shanghai, China

Correspondence

Jiangang Chen, No. 500 Dongchuan Road, Shanghai 200241, China.

Email: jgchen@cee.ecnu.edu.cn

Dean Ta, No. 2005 Songhu Road, Shanghai 200438, China.

Email: tda@fudan.edu.cn

Funding information

National Natural Science Foundation of China, Grant/Award Numbers: 12034005, 61975056; Natural Science Foundation of Shanghai, Grant/Award Number: 19ZR1416000; Science and Technology Commission of Shanghai Municipality, Grant/Award Numbers: 20440713100, 18DZ2270800; Shanghai Municipal Health Commission, Grant/Award Number: GWV-10.1-XK24; Shanghai Shenkang Hospital Management, Grant/Award Number: SHDC2020RC6030-002; CAMS Innovation Fund for Medical Sciences, Grant/Award Number: 2021-I2M-C&T-B-015; Shanghai Science and Technology Plan Project, Grant/Award Number: 21Y11902500; Shanghai Science and Technology Commission, Grant/Award Number: 20Z11900904

Abstract

Background: Auxiliary diagnosis and monitoring of lung diseases based on lung ultrasound (LUS) images is important clinical research. A-line is one of the most common indicators of LUS that can offer support for the assessment of lung diseases. A traditional A-line detection method mainly relies on experienced clinicians, which is inefficient and cannot meet the needs of these areas with backward medical level. Therefore, how to realize the automatic detection of A-line in LUS image is important.

Purpose: In order to solve the disadvantages of traditional A-line detection methods, realize automatic and accurate detection, and provide theoretical support for clinical application, we proposed a novel A-line detection method for LUS images with different probe types in this paper.

Methods: First, the improved Faster R-CNN model with a selection strategy of localization box was designed to accurately locate the pleural line. Then, the LUS image below the pleural line was segmented for independent analysis excluding the influence of other similar structures. Next, image-processing methods based on total variation, matched filter, and gray difference were applied to achieve the automatic A-line detection. Finally, the “depth” index was designed to verify the accuracy by judging whether the automatic measurement results belong to corresponding manual results ($\pm 5\%$). In experiments, 3000 convex array LUS images were used for training and validating the improved pleural line localization model by five-fold cross validation. 850 convex array LUS images and 1080 linear array LUS images were used for testing the trained pleural line localization model and the proposed image-processing-based A-line detection method. The accuracy analysis, error statistics, and Harsdorff distance were employed to evaluate the experimental results.

Results: After 100 epochs, the mean loss value of training and validation set of improved Faster R-CNN model reached 0.6540 and 0.7882, with the validation accuracy of 98.70%. The trained pleural line localization model was applied in the testing set of convex and linear probes and reached the accuracy of 97.88%

and 97.11%, respectively, which were 3.83% and 8.70% higher than the original Faster R-CNN model. The accuracy, sensitivity, and specificity of A-line detection reached 95.41%, 0.9244%, 0.9875%, and 94.63%, 0.9230%, and 0.9766% for convex and linear probes, respectively. Compared to the experienced clinicians' results, the mean value and p value of depth error were 1.5342 ± 1.2097 and 0.9021, respectively, and the Harsdorff distance was 5.7305 ± 1.8311 . In addition, the accumulated accuracy of the two-stage experiment (pleural line localization and A-line detection) was calculated as the final accuracy of the whole A-line detection system. They were 93.39% and 91.90% for convex and linear probes, respectively, which were higher than these previous methods.

Conclusions: The proposed method combining image processing and deep learning can automatically and accurately detect A-line in LUS images with different probe types, which has important application value for clinical diagnosis.

KEYWORDS

A-line detection, Faster R-CNN, gray difference, matched filter, TV filter

1 | INTRODUCTION

Being convenient, radiation-free, cost-effective, fast, and safe, ultrasound has been an effective means for the diagnosis of different clinical diseases.^{1,2} In recent years, lung ultrasound (LUS) is gaining increasing recognition as a useful tool for assessing lung pathophysiology. A decade of clinical and physical studies has clearly shown that LUS is able to detect lung diseases,^{2,3} such as pulmonary edema, pneumothorax, and chronic obstructive pulmonary disease, especially in the epidemic of the coronavirus disease-19 (COVID-19).⁴⁻⁷ The bedside LUS has become the only imaging equipment to enter the intensive care unit in the epidemic areas and played an important role in the real-time observation of lung disease development.⁸⁻¹⁴

In the LUS imaging, LUS scoring is commonly used to evaluate the clinical severity based on deep learning, which combined the A-lines, B-lines, pleural lines, and consolidation. However, these methods were based on the label scored by human vision and manual calculation,^{15,16} which have some similar limitations. For example, (1) lots of samples need to be labeled manually, which is time-consuming and labor-intensive; (2) manual scoring is subjective and experience dependent. They also may cause significant errors and have strong influence on the clinical diagnosis. Therefore, how to detect the A-lines, B-lines, and pleural lines automatically and independently is important for the LUS diagnosis in clinic.

Recently, there were many papers about the detection and extraction of B-lines and pleural lines, such as rough detection method, radon transform, and hidden Markov model,^{17-24,26} whereas the research of fast and accurate detection of A-line in different probe types is still under exploration. A-lines are kinds of linear hyper echo beneath and parallel to the pleural line, which are pro-

duced by multiple reflections of reverberation artifacts when the sound beam is perpendicular to the pleurae. Although the majority (94%) of healthy, nonsmoker elderly subjects (mean age 79-year old) showed no A-lines, A-lines always present in the LUS examinations of the healthy younger subjects (<50-year old).²⁵ Therefore, the consecutive pleural line and existent A-lines could be regarded as the important indicator to represent a healthy lung condition, serving as an important condition for the discharge of patients with COVID-19 pneumonia or other lung diseases.^{15,26} Although the detection of A-lines is more straightforward and easier than other LUS features, for example, B-lines, consolidation, it is not easy for the novice. Accurate detection also required special skills and rich experience in clinic.²⁷ Moreover, in special scenarios, such as battlefields, areas with poor health care, and even future home inspections, the fast, accurate, and automatic detection of A-lines is very important, which can preliminarily judge the possibility of a patient suffering from pneumonia, pneumothorax, or other diseases. It also improves the efficiency of medical auxiliary diagnosis. Therefore, it is also calling for the automatic detection of A-lines in LUS images.

In this aspect, some researchers focused on image analysis to achieve A-line detection in the past several years. Anantrasirichai et al.²¹ found the possible A-line occurrences according to the distance between skin and pleural lines. Karakus et al.²⁸ reconstructed the Radon space information via the Cauchy Proximal Splitting algorithm to detect the pleural line and roughly located A-lines by detecting those lines that parallel to the pleural line. Susanti et al.²⁹ proposed a pleural line extraction method based on morphological grayscale filter and adaptive low-pass filter with considering shape framework and then detected the A-line according to the parallel lines with fixed distance. These methods

depended on the measurement accuracy of the distance between pleural line and A-lines, which need to know the distance between skin and pleura in advance and require the high-quality LUS images. However, in most cases, due to the influence of clinician's manipulation, patient's posture, and other factors, the resolution of the acquired LUS images may not meet the needs of distance measurement. As a result, these methods were easily influenced by other similar structures and may produce some errors. What is more, Gare et al.³⁰ used the pretrained U-Net deep learning model for A-line detection, this method needed lots of labels for training, whereas the manual marking of A-lines was difficult and inefficient, which was also vulnerable to some similar structures.

For addressing these problems, we proposed a novel method in this paper for the automatic detection and analysis of A-lines. In detail, the proposed method consists of two stages. The first stage was the localization of the pleural line based on the improved faster region-based convolutional neural network (Faster R-CNN) model and the segmentation of region of interest (ROI) beneath the detected pleural line. The second stage was the automatic detection of A-lines, which was mainly based on the total variation (TV) filter and matched filter. The main contributions of this study can be summarized as follows:

1. The two-stage analysis method can effectively reduce the influence caused by other similar structures and directly analyze the ROI where A-lines located.
2. The combination of image processing algorithms can achieve the unsupervised detection for A-lines, which does not require high-quality LUS images and need to know in advance the distance from pleura line to skin surface, which facilitates the analysis of different scenes and different patients.
3. The proposed A-line detection method has good universality and can be widely used in LUS images of different probe types.

The paper is organized as follows. Section 2 illustrates the patients and methods. Section 3 reports the experiments and results. Section 4 addresses the discussion with Section 5 as the conclusion.

2 | METHODS

2.1 | Patients

The experiment involved 61 patients from two different hospitals. Among them, 31 patients were admitted to the Wuhan Huoshenshan Hospital and confirmed as COVID-19 pneumonia with computed tomography (CT, United Imaging, uCT760) and positive RT-PCR test.

The LUS images were collected by ultrasound equipment LOGIQ e (GE Healthcare, Wauwatosa, WI, USA), which was utilized and equipped with a convex probe of low frequency transducer (1–5 MHz). Another 30 patients were admitted to the Zhejiang University School of Medicine and confirmed as pneumothorax with CT. The LUS images were collected by the ultrasound equipment CX50 (Philips Healthcare, Bothell, US), which was utilized and equipped with convex and linear probe of central frequency transducer (7.5 MHz) for 25 and 5 patients, respectively. Considering that the patient number in this paper was not large, the analysis was given per image in this experiment. Clinicians usually analyze the lung disease by judging whether the A-lines existed in the real-time imaging video. Therefore, when the proposed method was used in a clinic, if A-line and pleural line are detected in some frames of the video, we can know that the patient's condition is improved.

In this experiment, a total of 3000 convex probe LUS images selected from different imaging regions of 39 patients (COVID-19 pneumonia: 31, pneumothorax: 8) were used for the training and validation of the proposed deep learning-based pleural line localization model. A total of 1930 LUS images (convex: 850; linear: 1080) collected from another 22 pneumothorax patients were used for the testing of the trained pleural line localization model and A-line detection method. There was no intersection between them. In other words, there were no two or more images with high similarity between the training set and the testing set. In addition, LUS images from the same scanning video were continuously selected at an interval of 10 frames to reduce the similarity among the adjacent images, for example, the 1st and 11th frames were selected as the first and second frame of the image for processing. They had the similarity less than 0.9, which was calculated by the entropy cross-correlation in the following equation:

$$S(A, B) = 1 - \left| \frac{E(A) - E(B)}{E(A)} \right| \quad (1)$$

$$E = \sum_{i=0}^{255} -P_i \log P_i$$

where E is the entropy of the collected image, P_i represents the proportion of pixels with gray value i in the image.

In this study, the gender, age, living environment, and past medical history were not considered. This study was approved by the Ethics Committee of Huoshenshan Hospital, Wuhan, China (Approval number: HSSL030) and the Ethics Committee of Affiliated Zhejiang Hospital, Zhejiang University School of Medicine, Hangzhou, China (Approval number: 310013).

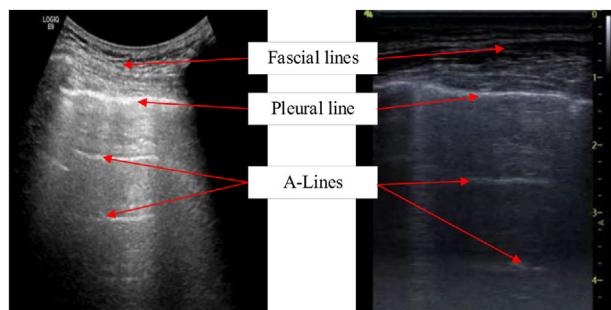


FIGURE 1 Structure schematic diagram of a LUS image

2.2 | Localization of pleural lines

There are some line objects shown in Figure 1 the pleural line such as fascial line, which are similar to the morphology of A-line and may be mistakenly recognized as the A-line, making the judgment of A-line of low confidence, especially for the novice. Therefore, it is necessary to prioritize the positioning of the pleural line before detecting the A-lines, so we can achieve the independent detection of the A-line in the area below the pleural line with less influence from other line objectives in LUS images.

Our previous pleural line detection method based on Radon transform mainly focused on the analysis of LUS images collected by linear probe, which could not directly analyze the LUS images collected by convex probe.²⁴ Carrer et al. proposed a pleural line detection method by combing a local scale hidden Markov model and the Viterbi algorithm for the analysis of LUS images collected by linear and convex probes, the results showed that the global accuracy for the convex case was less than the linear one, and it was also influenced by the image quality.²⁶ Inspired by these object detection tasks in the field of computer vision, we directly used the deep learning-based method to detect the pleural line region in LUS images, which cannot be affected by subjective and objective factors such as image quality. Therefore, in this paper, an improved Faster R-CNN deep learning model^{31,32} was designed to locate the pleural line automatically and accurately in those LUS images collected by convex and linear probes. The schematic diagram of this model is shown in Figure 2, which consists of five parts: feature extraction, region proposal network (RPN) model, ROI pooling, classifier, and selection strategy of localization box.

2.2.1 | Feature extraction

The backbone model was mainly composed of ResNet-50 model for the extraction of feature maps, which consists of conv and identify blocks, including convolution layer, pooling layer, batch normalization layer,

and ReLU activation function, and was applied for a subsequent RPN layer and a fully connected (FC) layer.

2.2.2 | RPN model

The model was mainly used to adjust and select the anchor boxes that were generated from the feature maps. These anchor boxes were first convoluted with a kernel size of 3×3 and ReLU activation function to increase the range of receptive field. Then, two different branches were generated for foreground classification and regression using the convolution layer with a kernel size of 1×1 , respectively. The upper branch contains 18 channels, whereas the next branch contains 36 channels. This is because for feature map, each pixel has nine anchors, two classifications (foreground/background), and four coordinate points for regression; thus, the upper one has 2×9 channels and the lower one has 4×9 channels. Next, the reshape layer was employed to adjust the matrix $[1, 2 \times 9, H, W]$ to $[1, 2, H \times 9, W]$, which can meet the needs of classification task with SoftMax. The second reshape was used to recover the matrix to an original shape. Finally, the proposal layer was used to select the positive anchor box using the intersection over union index. The non-maximum suppression algorithm was employed in this layer to select the most accurate proposal position.

2.2.3 | ROI pooling

This layer used the proposals generated by RPN and the feature map obtained by the last layer of ResNet-50 to get the proposal feature map with a fixed size. After entering the ROI pooling, it could use the FC operation to identify and locate the target.

2.2.4 | Classifier

The ROI pooling layer was formed into a fixed size feature map for FC operation. The SoftMax with cross-entropy loss function was used to classify specific categories. The smooth L1 loss was used to complete the bounding box region regression operation and obtain the accurate position of the object. The total loss function is shown in the following equation:

$$L(\{p_i\}, \{t_i\}) = \frac{1}{N_{cls}} \sum_i L_{cls}(p_i, p_i^*) + \lambda \frac{1}{N_{reg}} \sum_i p_i^* L_{reg}(t_i, t_i^*) \quad (2)$$

where p_i is the probability that the anchor is predicted as the target. t_i is a vector that represent anchor. N_{cls} and N_{reg} are the number of anchor and the size of feature map, respectively. λ is a constant representing the weight

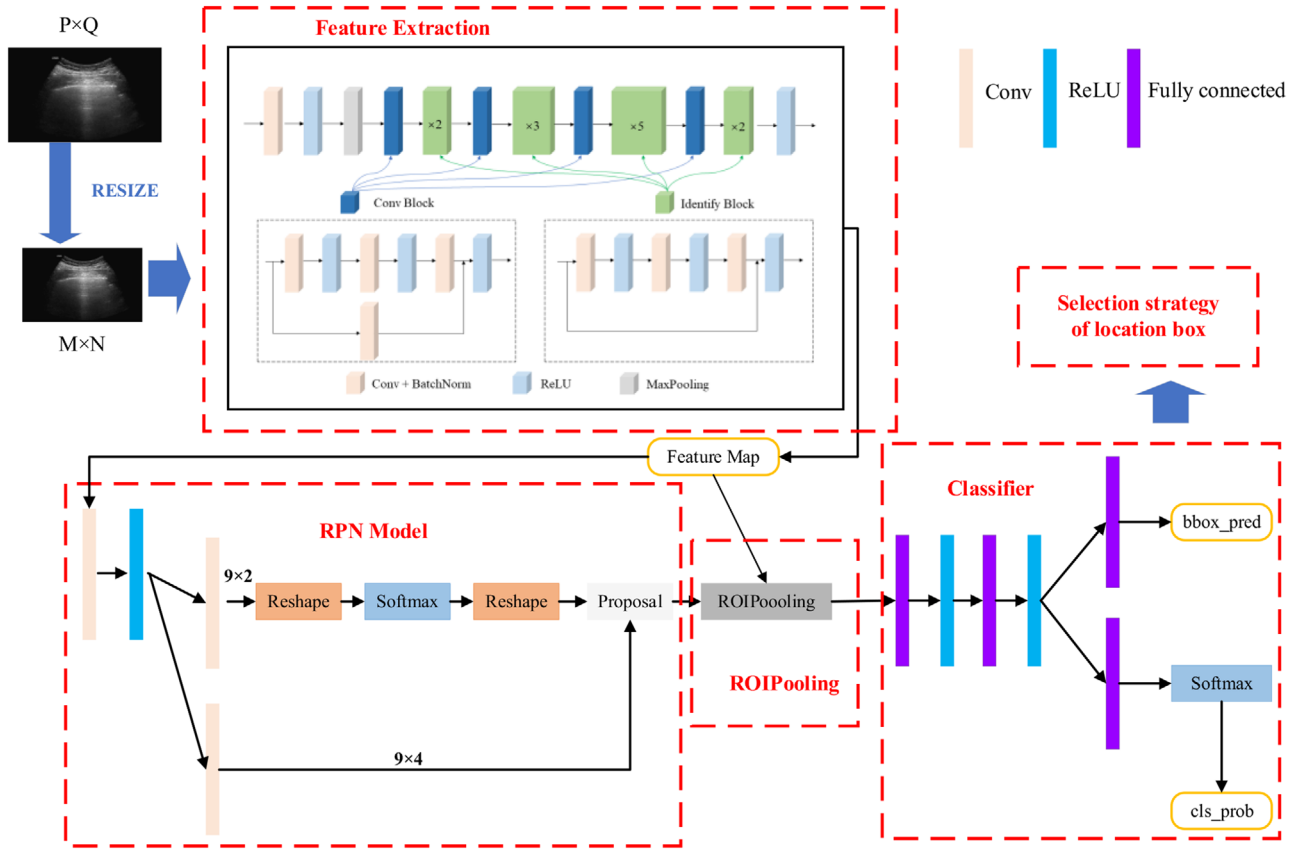


FIGURE 2 Schematic diagram of improved Faster R-CNN

of two loss and equal to 1 in this experiment. L_{cls} and L_{reg} are the cross-entropy loss and the smooth L1 loss, respectively, as shown in the following equation:

$$L_{cls}(p_i, p_i^*) = -\log[p_i^* p_i + (1 - p_i^*)(1 - p_i)] \quad (3)$$

$$L_{reg}(t_i, t_i^*) = \begin{cases} 0.5(t_i - t_i^*)^2 \times (1/\sigma^2) & \text{if } |t_i - t_i^*| < (1/\sigma^2) \\ |t_i - t_i^*| - 0.5 & \text{otherwise} \end{cases} \quad (4)$$

where σ is the constant used to control the smooth region and equal to 3 in this experiment.

2.2.5 | Selection strategy of localization box

Because A-lines are kinds of linear hyper echo of pleural lines, their morphological structures are similar to the pleural line, as a result of the previous steps, more than one localization box may be located, whereas there is only one for the pleural line. Thus, these erroneous results may have an impact on the second stage of the experiment. However, referring to clinical experience, the

real pleural line commonly has the highest recognition accuracy and minimum depth in the LUS images. (Depth refers to the distance between the pleural line and the surface of the skin, which is reflected in the ordinate at the position of the pleural line on the image.) Meanwhile, these similar structures, such as A-lines, commonly have the lower identification accuracy and higher depth than the real pleural lines. Therefore, according to this principle, a strategy shown in Figure 3 was proposed to improve the original Faster R-CNN model for selecting the only one correct pleural line localization box in the experimental task. Based on the experimental results from the improved Faster R-CNN model, if the box with the minimum depth and the box with the highest accuracy were the same, the detected object was considered the pleural line; otherwise, it was discarded.

2.3 | Automatic detection of A-lines

After the localization of the pleural line, the area below the localization box was segmented to obtain a new LUS image for the A-line detection and analysis. The matched filtering algorithm was used to process the denoised images that were preprocessed by the TV filter, and then we could get the candidates of the A-line.

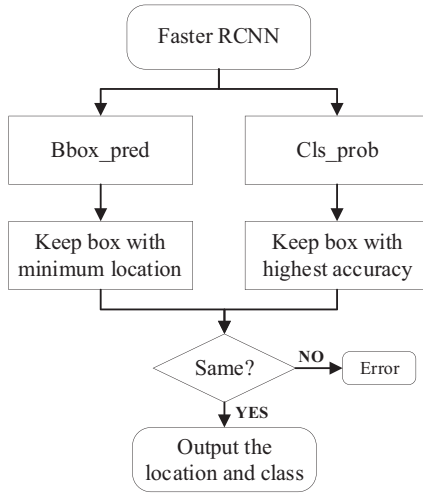


FIGURE 3 Flowchart of selection strategy

Furthermore, a gray difference algorithm was designed to compare the initial output A-lines and the original segmented image. As a result, the A-lines were finally detected with the pseudo-A-lines removed in the images outputted from the matched filter. The whole flowchart of A-line detection is shown in Figure 4.

2.3.1 | Image preprocessing

Image denoising is important for medical image analysis, especially for these ultrasound images with low resolution. Most denoising methods filter out important information such as edges, while filtering out noise information, such as Gaussian filtering algorithm and neighborhood filtering algorithm, which will affect the detection of A-lines. In our experiment, we fully consider the characteristics of local smoothing and nonlocal similarity, and the restore part of the original information on the basis of smoothing the images. Thus, we introduced the partial differential equation into the LUS image denoising task. As an important solution method, the TV filter^{33,34} was used for the initial LUS image denoising in the preprocessing process, whose mathematical model is shown as Equation (5), including regular term and fidelity term. The regularization term mainly plays the role of smoothing, and the fidelity term mainly reduces the image distortion by retaining the original image features. Its corresponding Euler–Lagrange partial differential equation is shown as follows:

$$J(u) = \min \iint_{\Omega} |\nabla u| dx dy + \frac{\lambda}{2} \iint_{\Omega} (u - u_0)^2 dx dy \quad (5)$$

$$-\nabla \left(\frac{\nabla u}{|\nabla u|} \right) + \lambda(u - u_0) = 0 \quad (6)$$

where u and u_0 are logarithm transformation of original image and mixed noise image, respectively. λ is the equilibrium parameters. Ω is the definition domain of image. $|\nabla u|$ is the L1 norm of the gradient vector. $1/|\nabla u|$ is the diffusion coefficient.

Because ∇u value of the edge is large, and the diffusion coefficient is small, the diffusion of edge direction is weak. The edge can be well preserved. However, in order to reduce the processing error caused by the model treating the noise as an edge region, the idea of isotropy was introduced into the original TV filter model. Thus, the novel isotropic diffusion model and the corresponding partial differential equation are shown as follows:

$$J(u)' = \min \frac{1}{2} \iint_{\Omega} |\nabla u|^2 dx dy + \frac{\lambda}{2} \iint_{\Omega} (u - u_0)^2 dx dy \quad (7)$$

$$-\nabla(\nabla u) + \lambda(u - u_0) = 0 \quad (8)$$

Therefore, the TV filter can de-noise the smooth area. Combining the characteristics of LUS image and A-line, this method denoised the LUS images and enhanced the A-lines.

2.3.2 | A-line detection

In the LUS images, the A-line a higher pixel gray value, whereas the upper and lower regions have a low pixel gray value; thus, it conforms to the Gaussian distribution in the vertical direction. Meanwhile, considering that the curvature of A-line is small and the thickness variation is small, we introduced matched filter algorithm^{35,36} with Gaussian kernel function to fit A-line. The areas in LUS image with high response that matched the filter scale may contain the candidates of the A-line. In order to match with the A-lines with different directions caused by the LUS imaging, the Gaussian kernel function was rotated using the rotation matrix to design the kernel function templates in different directions, as shown in the following equation:

$$K_i(x, y) = -\exp(-\mu^2/2\sigma^2), \forall \bar{p}_i \in N \quad (9)$$

$$N = \{(u, v) | |u| \leq 3\sigma, |v| \leq L/2\}$$

where (u, v) is the rotated coordinates. σ is the scale parameter of the filter, the 3σ contains most of the information. L is the length of the filter template assuming a fixed direction. $K_i(x, y)$ is the i th kernel function. N is the value range of neighborhood.

In addition, for making the filtering response of the filter template to the uniform background region zero, the kernel function was further modified to obtain

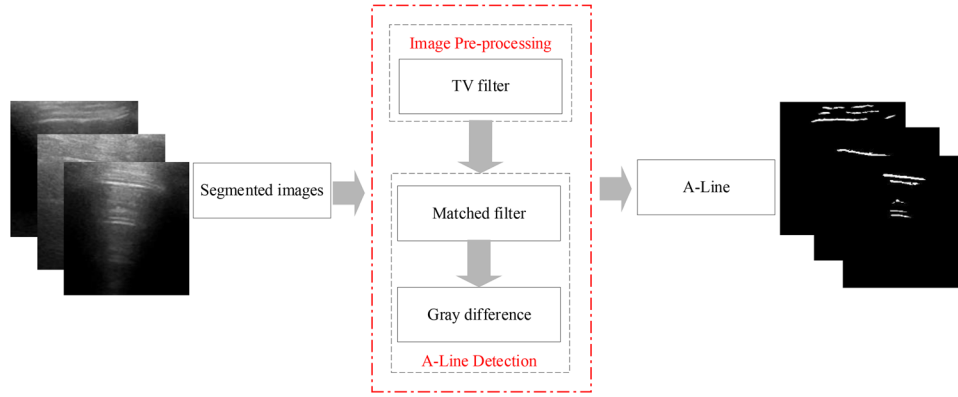


FIGURE 4 Flowchart of A-line detection

TABLE 1 Gray difference method

Discriminant Conditions	Results	Range of i and j
$I_{seg}(i,j) \geq P$	$I_{AL}(i,j) = I_{MF}(i,j)$	$i \in [1, N]$
$I_{seg}(i,j) < P$	$I_{AL}(i,j) = 0$	$j \in [1, M]$

Note: The size of segmented LUS image $I_{seg}(i,j)$ is $M \times N$. $I_{AL}(i,j)$ and $I_{PL}(i,j)$ are the final A-line image and the result image of matched filtering, respectively.

the final convolution mask, as shown in the following equation:

$$K'_i(x, y) = K_i(x, y) - A_i$$

$$A_i = \sum_{(u,v) \in N} K_i(x, y) / A$$
(10)

where A_i is the average value of kernel function. A is the number of pixels in N .

Therefore, when the output response of the matched filter exceeded the preset threshold, the pixel was marked as a part of A-line to achieve the purpose of extracting A-line. As a result, we got the initial detection results containing pseudo-A-lines. In addition, the gray difference method,³⁷ as shown in Table 1, was proposed to remove pseudo-A-line and obtain the final real A-line image. The output detection images from matched filter were fused with the segmented preprocessed images, if the gray value of A-lines at the position of the segmented image corresponding to the matched filter output images was higher than the preset threshold, it was the real A-line; otherwise, it was the pseudo-A-line.

2.3.3 | Validation of A-line detection method

We designed the “depth” index of A-lines to evaluate the accuracy of the proposed automatic detection method. This evaluation method mainly depended on whether

the depths of the existed A-line measured using the proposed method were close to the corresponding manual measurement ($\pm 5\%$). If all automatic measurement results were close to the corresponding manual measurement results, the detection was correct. If there was no corresponding manual measurement result for any automatic measurement result, the detection was wrong. The flowchart of the evaluation method was shown in Figure 5. The measurement of depth by the automated and manual method was shown in the following equation:

$$h_i = \sum_{p=1}^N y_p / N \quad p \in [1, N] \quad (11)$$

$$H_j = (C_1 + C_2) / 2 \quad (12)$$

where N is the number of pixels in the A-line, y_p is the depth of the p th pixel, C_1 and C_2 are the results from two different experienced clinicians.

3 | EXPERIMENTAL RESULTS

The proposed method has been tested on the data set collected from the 31 patients with COVID-19 pneumonia and 30 patients with pneumothorax. There were totally 4930 LUS images (convex: 3850; linear: 1080), and every two images were picked up from the same clip by every 20 frames to reduce the similarity between images, and we also used the entropy cross-correlation to ensure that the similarity of the two adjacent images from the same patient was less than 0.9, as shown in Table 2.

A number of 3000 convex probe LUS images collected from 39 patients were used for the training of the pleural line localization model, the fivefold cross-validation method was used to verify the trained model. Another 1930 LUS images (convex: 850, linear: 1080) collected from 22 patients were applied for testing the trained pleural line localization model and the proposed

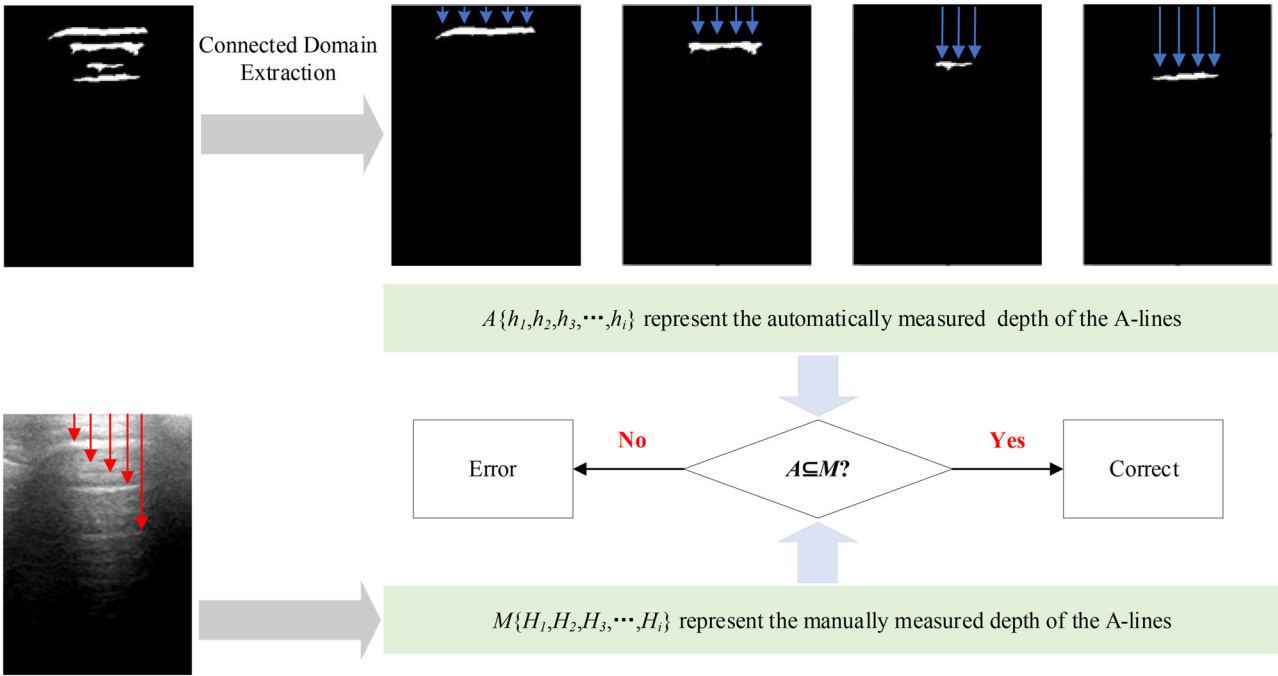


FIGURE 5 Flowchart of evaluation method

TABLE 2 Comparison of images in different frames of the same clip

Order	1	2	3
Example-1			
Entropy	4.41	3.86	5.11
Similarity (<0.9)	0.87	0.76	—
Example-2			
Entropy	5.56	4.06	4.90
Similarity (<0.9)	0.73	0.83	—

image processing-based A-lines detection method. In addition, the position of pleural line and A-lines was marked by two experienced clinicians (>6 years in using LUS). The depth measurement of A-line was performed by the two experienced clinicians, independently, with the

mean value as the gold standard. The image processing and deep learning were performed using MATLAB 2020a and Pytorch framework, respectively, running on a computer with a CPU: Intel Xeon Gold 6248R, RAM: 256G, GPU: Tesla V100.

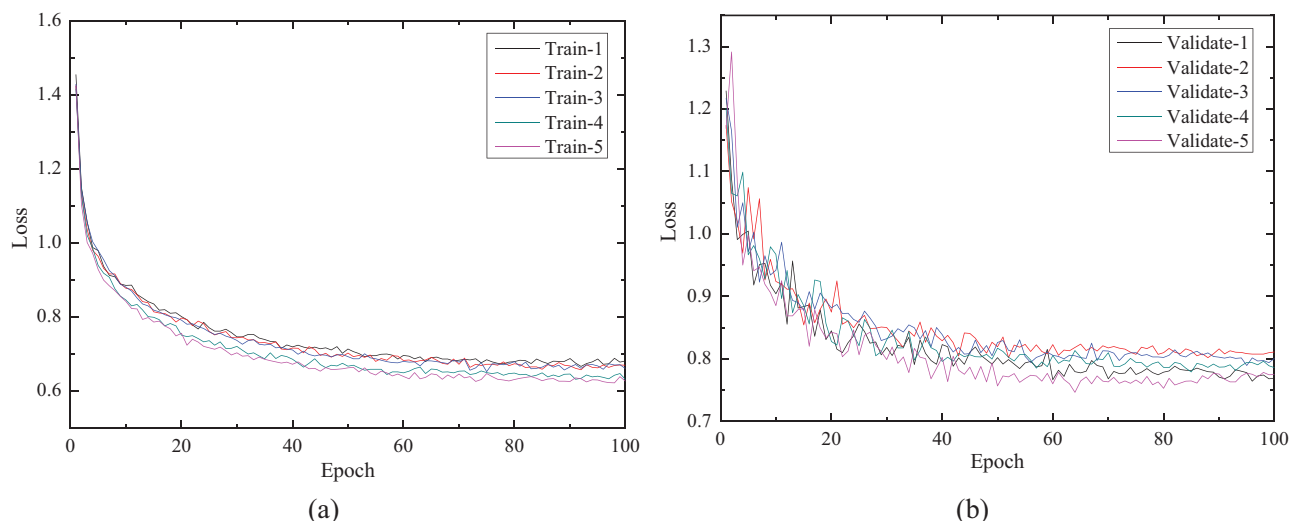


FIGURE 6 (a) Training loss and (b) validation loss of the Faster R-CNN model

TABLE 3 Experimental results of fivefold cross validation

Order	Loss		Accuracy (%)
	Train	Validation	
1	0.6814	0.7689	98.33
2	0.6697	0.8109	98.33
3	0.6610	0.8006	99.17
4	0.6315	0.7861	99.33
5	0.6268	0.7748	98.33
Average	0.6540	0.7882	98.70

3.1 | Localization of pleural lines

The improved Faster R-CNN model with ResNet-50 was used for the localization of pleural lines, the training parameters including epoch, batch size, learning rate, and optimizer were set as 100, 4, 0.0001, and Adam optimizer, respectively. A total of 3000 LUS images were randomly divided into 5 copies, each with 600 images. Four of them were selected for training, the other one for validation, and the experiment was repeated for five times. The experimental process and results were shown in Figure 6 and Table 3, respectively. The mean value of training and validation loss reached 0.6540 and 0.7882, respectively. The average validation accuracy of pleural line localization was 98.70%.

Another 1930 LUS images (convex: 850, linear: 1080), which were not involved in the training process of improving Faster R-CNN model, were used to test the trained model in each experiment, and the test results were shown in Table 4. It proved that the trained pleural line localization model could get the great effect with the accuracy of 97.88% and 97.11% for convex and linear probes, respectively. Through the proposal box, non-maximal suppression, and the proposed selection

TABLE 4 Experimental results in external data set

Probe type	Accuracy (%)					Average
	1	2	3	4	5	
Convex	97.76	97.76	98.11	98.00	97.76	97.88
Linear	96.48	96.39	97.41	97.69	97.59	97.11

strategy in Section 2.2, we obtained the final localization of the pleural line, as shown in Figure 7. However, there were some erroneous recognition results, which was because some A-lines closing to the pleural line were similar to the pleural line, and the recognition accuracy was higher than the real pleural line, resulting in false recognition after the proposed selection strategy, as shown in Figure 8.

In addition, the original Faster R-CNN model without the designed selection strategy of localization box was trained and tested using the same data set and fivefold cross-validation experiments; the experimental results were shown in Table 5, with the accuracy for convex probe images and linear probe images being 94.05% and 88.41%, respectively, which was lower than the improved Faster R-CNN model in this paper.

3.2 | Detection of A-lines

After the localization of the pleural line, we cut out the area beneath the pleural line for the detection of A-lines. This operation reduced the influence of some similar structure from other regions. Taking the linear probe and convex probe LUS images shown in Figure 9a as an example, the segmented images (Figure 9b) were first processed by the TV filter, which denoised the smooth area and preserved the edge area in LUS images. Then, the denoised LUS images (Figure 9c)

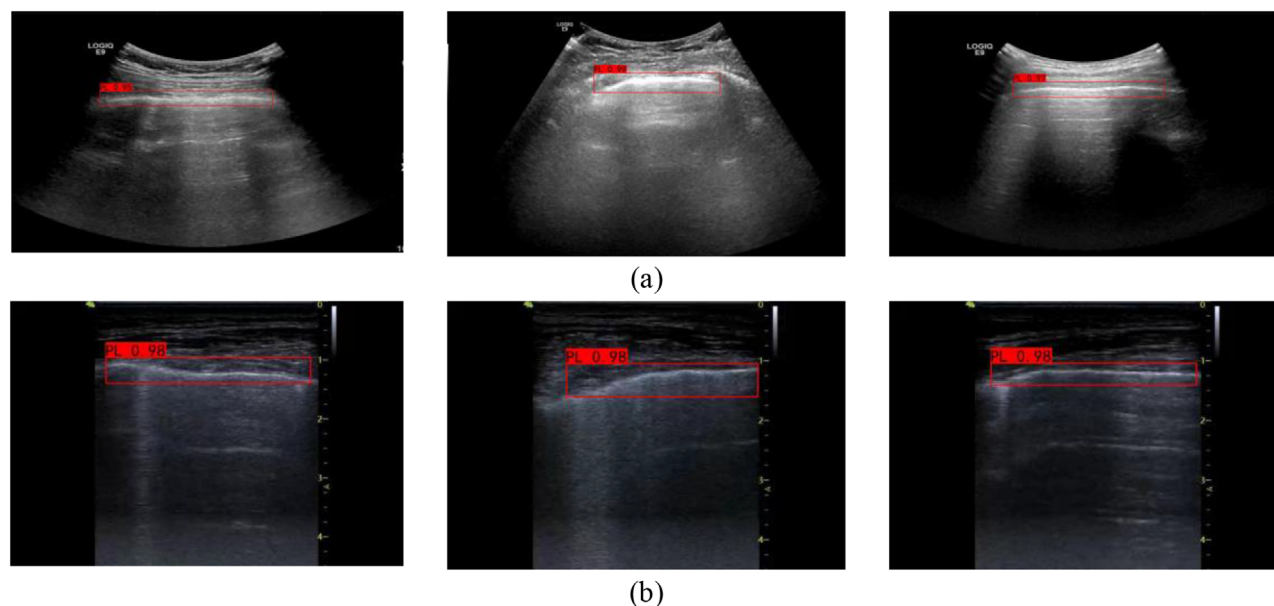


FIGURE 7 Detection results of pleural line: (a) convex and (b) linear

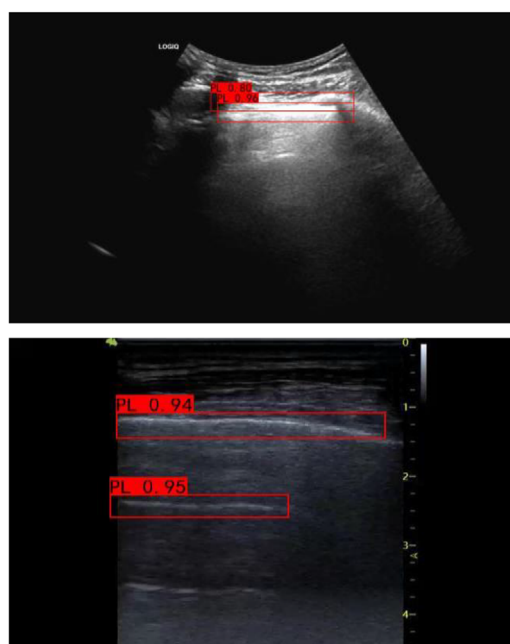


FIGURE 8 Wrong recognition of multiple pleural lines

were subsequently put into the matched filter with the scale parameter, the length of the filter template, and the numbers of rotation angle were 3, 5 (fine-tuning may be required in some images), and 12, respectively. The output of matched filter was shown in Figure 9d. Next, by comparing the result image and segmented image, it could be seen that there were some lines marked with red boxes that may not belong to the real A-line. Therefore, the gray difference method was applied for the result image of matched filter and the

TABLE 5 Experimental results of original Faster R-CNN model

Probe type	Accuracy (%)					Average
	1	2	3	4	5	
Convex	94.00	93.53	94.71	94.24	93.76	94.05
Linear	87.87	88.06	88.70	88.98	88.43	88.41

segmented image, we could remove the pseudo-A-line in the output images of matched filter, as shown in Figure 9e,f. As a result, we could get the final real A-lines accurately.

Meanwhile, the experiment results for those LUS images without A-lines by using the proposed method were shown in Figure 10. There were no A-lines in experimental result images, which was consistent with the facts. Thus, the proposed A-line detection method also can accurately determine the absence of A-line.

All images in the testing set of pleural line localization were used to verify the image processing-based A-line detection method. The correct images of pleural line recognition were directly cropped to obtain the lower region, and the wrong images were manually cropped to obtain the lower region. A total of 1930 segmented LUS images were employed in the experiment of A-line detection and evaluation. Among them, the number of convex probe LUS images was 850, with 450 images containing A-lines. The number of linear probe LUS images was 1080, with 610 images containing A-lines. All detection results were validated by the index of “depth.” Meanwhile, we used three indexes, including accuracy (*ACC*), sensitivity (*SEN*), and specificity (*SPE*) (Equations 13–15) to evaluate the detection method. The experimental results were shown in Table 6. The

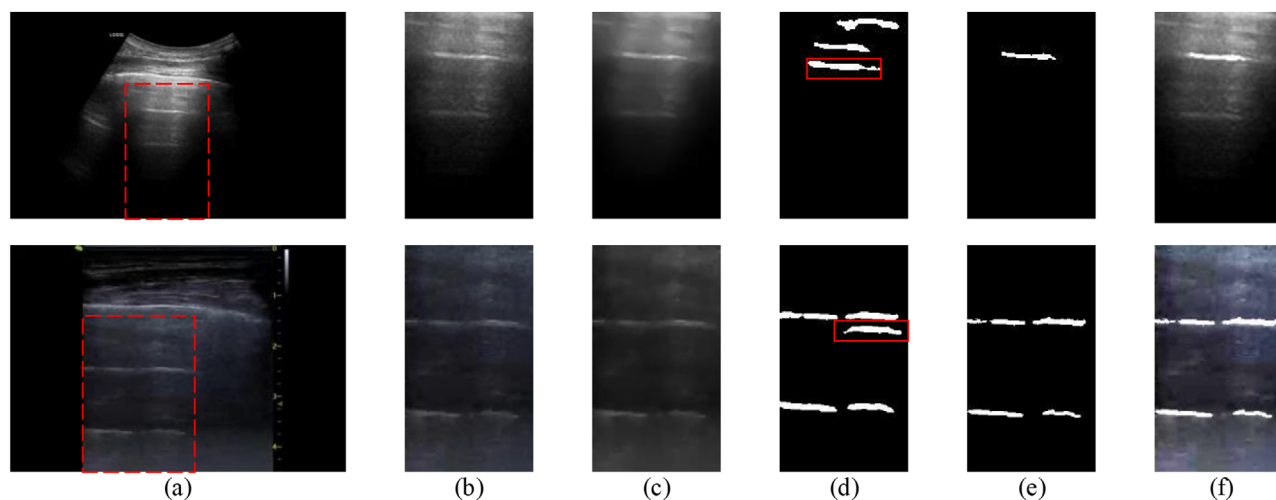


FIGURE 9 Process images of A-line detection (the process images were displayed in the same size): (a) original image; (b) segmented image; (c) TV filter; (d) matched filter; (e) gray difference; and (f) final result

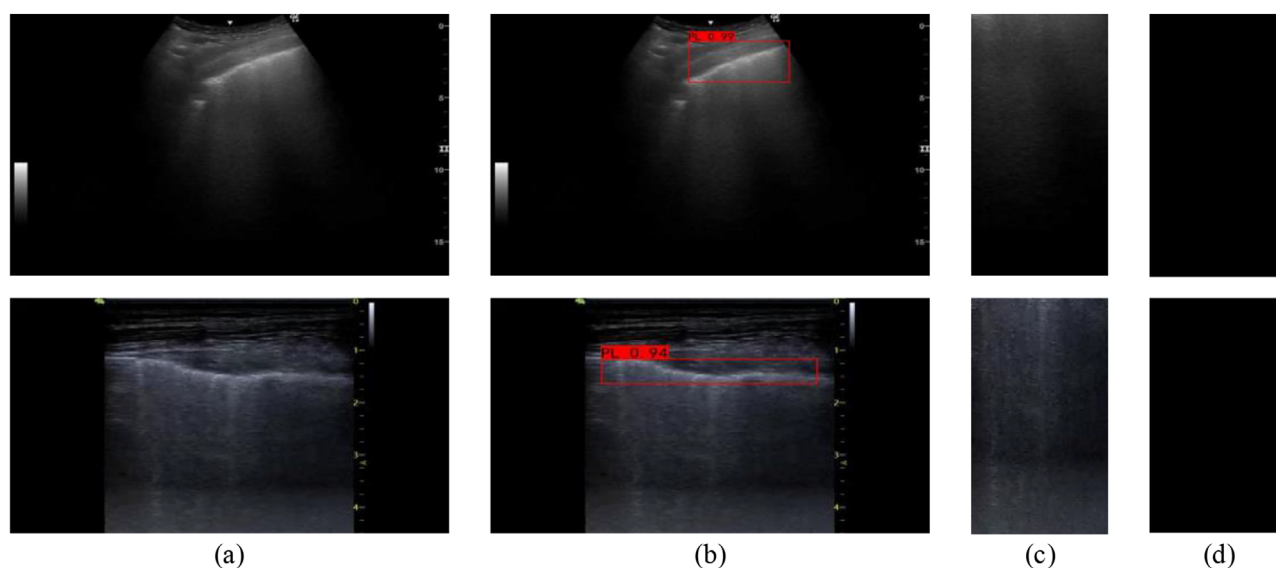


FIGURE 10 Detection process and results of the LUS images without A-lines: (a) original image; (b) pleural line localization; (c) segmented image; and (d) final result

accuracy, sensitivity, and specificity of A-line detection reached 95.41%, 0.9244, 0.9875, and 94.63%, 0.9230, 0.9766 for convex and linear probe images, respectively:

$$ACC = \frac{TP + TN}{TP + TN + FP + FN} \quad (13)$$

$$SEN = \frac{TP}{TP + FN} \quad (14)$$

$$SPE = \frac{TN}{TN + FP} \quad (15)$$

where TP , TN , FP , and FN are true positives, true negatives, false positives, and false negatives, respectively.

TABLE 6 A-line detection results of testing set

Results	Convex probe image		Linear probe image	
	A-line	Without A-line	A-line	Without A-line
Total	450	400	610	470
All correct identification	416	395	563	459
Include error identification	27	5	38	11
Unrecognized	7	/	9	/
Accuracy (%)	95.41		94.63	
Sensitivity	0.9244		0.9230	
Specificity	0.9875		0.9766	

TABLE 7 Statistical analysis of partially identified correct A-lines

Index		Clinician-1	Clinician-2	Average
Error statistics	Mean value	1.5897	1.4786	1.5342
	Standard	1.2045	1.2148	1.2097
	<i>p</i> Value	0.9131	0.8889	0.9021
Harsdorff distance	Mean value	5.4696	5.9914	5.7305
	Standard	1.7435	1.9186	1.8311

Note: *p* Value represents the statistics difference of two methods, and there is statistical significance when the value is less than 0.05.

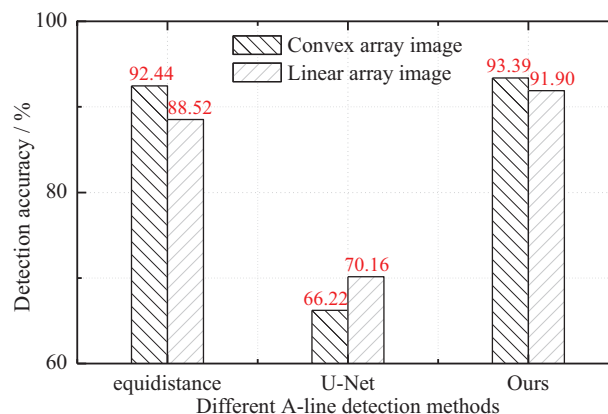
For these correctly identified A-lines, the error of depth measured by the automatic method and its corresponding manual measurement results measured by two different experienced clinicians was analyzed using mean value, standard, and *p* value in the experiments. Meanwhile, the Harsdorff distance was adopted to analyze the similarity between the automatically detected A-line and the manually drawn by two experienced clinicians. Experimental results were shown in Table 7. In these successful cases, the errors all were below 5% with the average \pm standard and *p* value of 1.5342 ± 1.2097 and 0.9021, respectively. The average \pm standard of Harsdorff distance was 5.7305 ± 1.8311 . They all proved that the proposed A-line detection had good performance.

3.3 | Comparison with other methods

For evaluating the whole system of A-line automatic detection, the accumulated error of the two-stage (pleural line localization and A-line detection) was calculated in the experiment, which was 6.61% and 8.10% for convex and linear probes, respectively. In other words, the final accumulated accuracy of the whole system was 93.39% and 91.90% for convex and linear probes, respectively. In addition, we compared our method with two main detection methods using the same LUS testing set, including the equidistance method proposed by Anantrasirichai et al.²¹ and the U-Net detection method proposed by Gare et al.³⁰ Their detection accuracies all were evaluated using the “depth” index introduced in Section 2.3.3, whose experimental results were shown in Figure 11. The comparison results showed that our method was better than the previous classical methods on both linear array and convex array probes.

4 | DISCUSSION

In this study, we developed a novel method for the automatic detection of the A-lines using deep learning and image processing methods. The innovations of the proposed method were summarized as follows: (1) It was not affected by the type of imaging probe and had good

**FIGURE 11** Comparison of different A-line detection methods

robustness. (2) It reduced the influence of human intervention or objective factors and improved the detection accuracy. With further tests on the large number of data set, the proposed method may have high applicability and improve the efficiency of the clinical procedures.

As we all know, the Faster R-CNN model has a stable performance in object detection, in this experiment, its accuracy in the pleural line localization was 94.05% and 88.41% for convex and linear probes in testing set, respectively. However, there were some structures similar to pleural lines in LUS images, such as A-line, it may lead to some erroneous recognition of multiple pleural lines. Therefore, we proposed the selection strategy of localization box after Faster R-CNN effectively to solve the previous problems and obtained more accurate pleural line localization results, with the accuracy of 97.88% and 97.11% for convex and linear probe LUS images in testing set, respectively. Meanwhile, compared with our previous pleural line detection method based on radon transform,²⁴ the proposed deep learning-based method had better performance, no matter what type of LUS images. It also showed good predictability even if the contrast of pleural line in the LUS image was not high and was least interfered by other reflection interfaces, such as the muscle fibers, fat-muscle interface. In addition, the accurate localization of pleural line also provides effective help for the subsequent analysis of pleural line segmentation and thickness measurement. A-line detection data set contained 1930 LUS images, including linear and convex probe images, as well as images with and without A-line. These experimental results shown in Figures 9 and 10 confirmed that this image-processing-based method had a good effect on detecting A-lines in LUS images in the aspect of image representation. At the same time, quantitative analysis of detection accuracy including accuracy, sensitivity, specificity, error statistics, and Harsdorff distance shown in Tables 6 and 7 also proved the proposed method had great performance and close to the clinicians' judgment. In addition, because our method was composed

of two stages: pleural line localization and A-line detection; thus, we employed the accumulated accuracy of the two-stage to evaluate the error of whole system in the experiment, the results showed that our method was less affected by image quality and had higher A-line detection accuracy compared with Anantrasirichai's equidistance method²¹ and Gare's U-Net method.³⁰

What is more, this method adopted the non-radiative and noninvasive automatic diagnosis image-based method for the A-line and pleural line detection to obtain the accurate characteristics of lung status. Compared with these inspection methods, including chest CT,^{38,39} chest X-ray,⁴⁰ and blood test,⁴¹ the proposed method provided a novel idea that was more convenient, fast, and suitable for clinical application.

Above all, the method proposed in this paper had good effect and robustness for detection of pleural line and A-lines. It could not only help the inexperienced clinicians to diagnose some clinic disease, such as pneumonia and pneumothorax, but also built the confidence when the automatic approach agrees with the visual.

There are some limitations of the study. First, the image-processing algorithms involved in this paper need to be set the certain threshold. It was commonly set by the empiric value and may cause some error on the detection result of A-line. Second, considering the failure cases in this study, the proposed method may need to be improved for these LUS with serious rupture of pleural line. Third, the absence of A-lines is not mutually exclusive to the presence of B-lines or other pathologic conditions, the automatic detection of A-lines should consider other LUS indicators. In the future, we will improve the proposed method to design more advanced image-processing algorithm with adaptive threshold and collect more ultrasound images, including convex or linear probe, multicenter, and multistructure to verify this A-line detection model and achieve best performance. We will also study other LUS indicators and explore the detection or localization of the artifactual patterns associated with pathological conditions to better meet the clinical needs.

5 | CONCLUSION

The detection of A-lines is important for the auxiliary diagnosis of LUS in clinic. In this paper, we proposed an automatic A-line detection method based on deep learning and image-processing methods, which consists of Faster R-CNN model, TV filter, matched filter, and gray difference. The designed method was evaluated in the self-defined LUS data set from different probe types, patients, diseases, and hospitals. Experimental results showed that the method had a good performance, which was close to the gold standard and better than the previous methods. However, these existed limitations also require us to improve this method and test

on more diverse data set in the future study. Ultimately, this method is potentially applicable to the clinic on various occasions.

ACKNOWLEDGMENTS

This work was supported in part by National Natural Science Foundation of China (Nos. 12034005 and 61975056), Shanghai Natural Science Foundation (No. 19ZR1416000), Science and Technology Commission of Shanghai Municipality (Nos. 20440713100, 19511120100, and 18DZ2270800), Shanghai Municipal Health Commission (No. GWV-10.1-XK24), Shanghai Shenkang Hospital Management (No. SHDC2020CR6030-002), CAMS Innovation Fund for Medical Sciences (No. 2021-I2M-C&T-B-015), Shanghai Science and Technology Plan Project (No. 21Y11902500), and Shanghai Science and Technology Commission (No. 20Z11900904).

CONFLICT OF INTEREST

The authors have no relevant conflicts of interest to disclose.

REFERENCES

- Chen J, He C, Yin J, et al. Quantitative analysis and automated lung ultrasound scoring for evaluating COVID-19 pneumonia with neural networks. *IEEE Trans Ultrason Ferroelectr Freq Control*. 2021;68(7):2507-2515.
- Mayo PH, Copetti R, Feller-Kopman D, et al. Thoracic ultrasonography: a narrative review. *Intensive Care Med*. 2019;45(9):1200-1211.
- Bouhemad B, Brisson H, Le-Guen M, Arbelot C, Lu Q, Rouby JJ. Bedside ultrasound assessment of positive end-expiratory pressure-induced lung recruitment. *Am J Respir Crit Care Med*. 2011;183(3):341-347.
- Soldati G, Smargiassi A, Inchingolo R, et al. Proposal for international standardization of the use of lung ultrasound for patients with COVID-19: a simple, quantitative, reproducible method. *J Ultrasound Med*. 2020;39(7):1413-1419.
- Allinovi M, Parise A, Giacalone M, et al. Lung ultrasound may support diagnosis and monitoring of COVID-19 pneumonia. *Ultrasound Med Biol*. 2020;46(11):2908-2917.
- La Salvia M, Secco G, Torti E, et al. Deep learning and lung ultrasound for Covid-19 pneumonia detection and severity classification. *Comput Biol Med*. 2021;136:104742-104742.
- Pecho-Silva S, Claudia Navarro-Solsol A, Taype-Rondan A, et al. Pulmonary ultrasound in the diagnosis and monitoring of coronavirus disease (COVID-19): a systematic review. *Ultrasound Med Biol*. 2021;47(8):1997-2005.
- Buonsenso D, Raffaelli F, Tamburrini E, et al. Clinical role of lung ultrasound for diagnosis and monitoring of COVID-19 pneumonia in pregnant women. *Ultrasound Obstet Gynecol*. 2020;56(1):106-109.
- Hussain A, Via G, Melniker L, et al. Multi-organ point-of-care ultrasound for COVID-19 (PoCUS4COVID): international expert consensus. *Crit Care*. 2020;24(1):702.
- Ji L, Cao C, Gao Y, et al. Prognostic value of bedside lung ultrasound score in patients with COVID-19. *Crit Care*. 2020;24(1):700.
- Li W, Fu ML, Qian C, et al. Quantitative assessment of COVID-19 pneumonia in neonates using lung ultrasound score. *Pediatr Pulmonol*. 2021;56:1419-1426.
- Mento F, Perrone T, Macioce VN, et al. On the impact of different lung ultrasound imaging protocols in the evaluation of patients

- affected by coronavirus disease 2019 how many acquisitions are needed? *J Ultrasound Med*. 2021;40(10):2235-2238.
13. Yu ACH, Demi L, Muller M, Zhou QF. Ultrasound imaging: a silent hero in COVID-19 and lung diagnostics. *IEEE Trans Ultrason Ferroelectr Freq Control*. 2020;67(11):2194-2196.
 14. Zhao L, Yu K, Zhao Q, et al. Lung ultrasound score in evaluating the severity of coronavirus disease 2019 (COVID-19) pneumonia. *Ultrasound Med Biol*. 2020;46(11):2938-2944.
 15. Soldati G, Demi M, Smargiassi A, Inchingolo R, Demi L. The role of ultrasound lung artifacts in the diagnosis of respiratory diseases. *Expert Rev Respir Med*. 2019;13(2):163-172.
 16. Zhu ST, Tao FY, Xu JH, et al. Utility of point-of-care lung ultrasound for clinical classification of COVID-19. *Ultrasound Med Biol*. 2021;47(2):214-221.
 17. van Sloun RJG, Demi L. Localizing B-lines in lung ultrasonography by weakly supervised deep learning, in-vivo results. *IEEE J Biomed Health Inf*. 2020;24(4):957-964.
 18. Brusasco C, Santori G, Bruzzo E, et al. Quantitative lung ultrasonography: a putative new algorithm for automatic detection and quantification of B-lines. *Crit Care*. 2019;23(1):288.
 19. Brattain LJ, Telfer BA, Liteplo AS, Noble VE. Automated B-line scoring on thoracic sonography. *J Ultrasound Med*. 2013;32(12):2185-2190.
 20. Moshavegh R, Hansen KL, Moller-Sorensen H, Nielsen MB, Jensen JA. Automatic detection of B-lines in in vivo lung ultrasound. *IEEE Trans Ultrason Ferroelectr Freq Control*. 2019;66(2):309-317.
 21. Anantrasirichai N, Hayes W, Allinovi M, Bull D, Achim A. Line detection as an inverse problem: application to lung ultrasound imaging. *IEEE Trans Med Imaging*. 2017;36(10):2045-2056.
 22. Anderson KL, Fields JM, Panebianco NL, et al. Inter-rater reliability of quantifying pleural b-lines using multiple counting methods. *J Ultrasound Med*. 2013;32(1):115-120.
 23. Roy S, Menapace W, Oei S, et al. Deep learning for classification and localization of COVID-19 markers in point-of-care lung ultrasound. *IEEE Trans Med Imaging*. 2020;39(8):2676-2687.
 24. Chen J, Li J, He C, Li W, Li Q. Automated pleural line detection based on radon transform using ultrasound. *Ultrason Imaging*. 2021;43(1):19-28.
 25. Chiesa AM, Ciccarese F, Gardelli G, et al. Sonography of the normal lung: comparison between young and elderly subjects. *J Clin Ultrasound*. 2015;43(4):230-234.
 26. Carrer L, Donini E, Marinelli D, et al. Automatic pleural line extraction and COVID-19 scoring from lung ultrasound data. *IEEE Trans Ultrason Ferroelectr Freq Control*. 2020;67(11):2207-2217.
 27. Lichtenstein DA, Meziere GA, Lagoueyte JF, Biderman P, Goldstein I, Gepner A. A-lines and B-lines lung ultrasound as a bedside tool for predicting pulmonary artery occlusion pressure in the critically ill. *Chest*. 2009;136(4):1014-1020.
 28. Karakus O, Anantrasirichai N, Aguersif A, Silva S, Basarab A, Achim A. Detection of line artifacts in lung ultrasound images of COVID-19 patients via nonconvex regularization. *IEEE Trans Ultrason Ferroelectr Freq Control*. 2020;67(11):2218-2229.
 29. Susanti H, Suprijanto. Image processing framework for pleural line (A-line) detection in video lung ultrasonography. 2020 IEEE-EMBS Conference on Biomedical Engineering and Sciences, Electr Network, IEEE; 2021:99-102.
 30. Gare GR, Schoenling A, Philip V, et al. Dense pixel-labeling for reverse-transfer and diagnostic learning on lung ultrasound for Covid-19 and pneumonia detection. 2021 IEEE 18th International Symposium on Biomedical Imaging, France, IEEE; 2021:1406-1410.
 31. Ren S, He K, Girshick R, Sun J. Faster R-CNN: towards real-time object detection with region proposal networks. *IEEE Trans Pattern Anal Mach Intell*. 2017;39(6):1137-1149.
 32. Wan SH, Goudos S. Faster R-CNN for multi-class fruit detection using a robotic vision system. *Comput Netw*. 2020;168:6.
 33. Rudin LI, Osher S, Fatemi E. Nonlinear total variation based noise removal algorithms. *Physica D*. 1992;60(1-4):259-268.
 34. Huang Q, Yang F, Liu L, Li X. Automatic segmentation of breast lesions for interaction in ultrasonic computer-aided diagnosis. *Inf Sci*. 2015;314, 293-310.
 35. Xing WY, Deng N, Xin BJ, Liu YW, Chen Y, Zhang ZY. Identification of extremely similar animal fibers based on matched filter and HOG-SVM. *IEEE Access*. 2019;7:98603-98617.
 36. Chaudhuri S, Chatterjee S, Katz N, Nelson M, Goldbaum M. Detection of blood-vessels in retinal images using two-dimensional matched-filters. *IEEE Trans Med Imaging*. 1989;8(3):263-269.
 37. Liu YW, Liu X, Wang SH, Song JL, Zhang JQ. A novel method for accurate extraction of liver capsule and auxiliary diagnosis of liver cirrhosis based on high-frequency ultrasound images. *Comput Biol Med*. 2020;125:15.
 38. Zhao WX, Lu M, Wang XM, Guo Y. The role of sarcopenia questionnaires in hospitalized patients with chronic heart failure. *Aging Clin Exp Res*. 2021;33(2):339-344.
 39. Zhao C, Xu Y, He Z, et al. Lung segmentation and automatic detection of COVID-19 using radiomic features from chest CT images. *Pattern recognit*. 2021;119:108071.
 40. Alhudhaif A, Polat K, Karaman O. Determination of COVID-19 pneumonia based on generalized convolutional neural network model from chest X-ray images. *Expert Syst Appl*. 2021;180:9.
 41. Pulgar-Sanchez M, Chamorro K, Fors M, et al. Biomarkers of severe COVID-19 pneumonia on admission using data-mining powered by common laboratory blood tests-datasets. *Comput Biol Med*. 2021;136:104738-104738.

How to cite this article: Xing W, Li G, He C, et al. Automatic detection of A-line in lung ultrasound images using deep learning and image processing. *Med Phys*. 2023;50:330–343. <https://doi.org/10.1002/mp.15908>